

Discrete Boltzmann modeling of Rayleigh-Taylor instability in bi-component compressible flows

Chuandong Lin^{a,b,1}, Aiguo Xu^{c,d,2}, Guangcai Zhang^c, Kaihong Luo^{b,e},
Yingjun Li^{b,3}

^a*State Key Laboratory for GeoMechanics and Deep Underground Engineering, China
University of Mining and Technology, Beijing 100083, China*

^b*Center for Combustion Energy, Key Laboratory for Thermal Science and Power
Engineering of Ministry of Education, Department of Thermal Engineering, Tsinghua
University, Beijing 100084, China*

^c*Laboratory of Computational Physics, Institute of Applied Physics and Computational
Mathematics, P. O. Box 8009-26, Beijing 100088, China*

^d*Center for Applied Physics and Technology, MOE Key Center for High Energy Density
Physics Simulations, College of Engineering, Peking University, Beijing 100871, China*

^e*Department of Mechanical Engineering, University College London, Torrington Place,
London WC1E 7JE, UK*

Abstract

A discrete Boltzmann model (DBM) is proposed and applied to probe Rayleigh-Taylor (RT) instability in bi-component compressible flows. The two components, whose specific heat ratios are independent, are described by two coupled discrete Boltzmann equations. Two types of the force term, which are equivalent at the level of the first order accuracy, are introduced to describe the gravitational effects. The discrete velocities for the two discrete Boltzmann equations are independent. Apart from its capability of a Navier-Stokes model describing the fluid flow, the DBM can also be employed to probe more details of non-equilibrium manifestations, which can be expressed in mathematical forms of tensors as well as their invariants. We investigate the global effects of the “fluctuation of translational energies” and “non-organized energy flux”, and the growth rate of the entropy of mixing in the evolution of RT instability. It is interesting to find that, for low Reynolds numbers, they show decreasing, in-

¹Corresponding author. Email addresses: chuandonglin@163.com

²Corresponding author. Email addresses: Xu_Aiguo@iapcm.ac.cn

³Corresponding author. Email addresses: lyj@aphy.iphy.ac.cn

creasing, and then decreasing trends. For high Reynolds numbers, the early reducing tendency is particularly suppressed and even eliminated. The competitive effects on non-equilibrium manifestations and growth of mixing entropy in the process are studied.

Keywords: Discrete Boltzmann model, Rayleigh-Taylor instability,

Non-equilibrium effects, Entropy of mixing

PACS: 47.11.-j, 47.20.-k, 47.55.-t, 51.10.+y

1. Introduction

Rayleigh-Taylor (RT) instability [1, 2] occurs when a heavy fluid is accelerated or supported by a light one in a force field. It is viewed as one of the most fundamental and ubiquitous forms of interfacial instability between fluids with different densities [3]. It covers a wide range of applications and objects, from microscopic to macroscopic level, such as inertial confinement fusion [4], astrophysics [5], atmospheric science [6], oceanography [7], combustion [8, 9], etc. Extensive efforts have been devoted to theoretical [10, 11], experimental [12, 13], and computational [14, 15] researches. At present, it is still an open subject with many challenging issues, especially those relevant to hydrodynamic non-equilibrium (HNE) and thermodynamic non-equilibrium (TNE) [14, 15] behaviors in non-equilibrium environments [16]. To investigate those complex non-equilibrium manifestations, a feasible method is to employ the Boltzmann equation which describes the evolution of non-equilibrium statistical physical systems.

Over the last three decades, the lattice Boltzmann method (LBM), which is based on the Boltzmann equation, [17, 18, 19, 20, 21, 22] has emerged as a versatile computational tool for dynamics of complex systems, including the RT instability [23, 24, 25, 26, 27, 28, 29, 30, 31, 32, 33]. These works [23, 24, 25, 26, 27, 28, 29, 30, 31, 32, 33] mainly focused on the RT instability in mono-component fluids with cold (hot) region on the top (bottom) half. For a more practical case, where the temperature in the two halves can be the same

or different, models suitable for bi- or multi-component flows are preferable [34, 35]. In 1998, Nie et al. [34] used an LBM for multi-component systems to simulate the Rayleigh-Taylor instability. The evolution of the instability in the linear and mixing stages is successfully simulated. In 2013, based on the phase-field theory, Zu and He [35] presented an LBM for incompressible binary fluids with density and viscosity contrasts. This model has the capability of simulating bi-component system with moderate density ratios.

However, previous LBMs are just solvers of traditional hydrodynamic equations, such as Navier-Stokes (NS) equations. To obtain a deeper insight into both the HNE and TNE effects that are beyond the description of traditional hydrodynamic models, we resort to the lattice Boltzmann kinetic method which is also named discrete Boltzmann method (DBM) [14, 15, 36, 37, 38, 39, 40, 41, 42, 43]. In 2016, via the DBM, Lai et al. [14] probed the effects of compressibility on RT instability by inspecting the interplay between HNE and TNE phenomena. Almost at the same time, Chen et al. [15] investigated the viscosity, heat conductivity, and Prandtl number effects from macroscopic and non-equilibrium viewpoints by using a multiple-relaxation-time DBM. The two DBMs [14, 15] are only applicable to single component fluids. Up to now, no DBM for a binary mixture in a force field is presented. In this work, we extend the DBM for compressible bi-component systems and study the dynamic process of non-equilibrium RT instability.

The rest of the paper is organized as follows. In Sec. 2, the proposed DBM is validated theoretically that it has the capability of NS models describing fluid flows in the hydrodynamic limit. In Sec. 3, it is further verified numerically, and then used to simulate the RT instability. The entropy of mixing and some non-equilibrium manifestation are investigated in the evolution of the RT instability. Section 4 gives conclusion and discussion.

2. Discrete Boltzmann Equation

Recently, a DBM [42] has been presented for the system containing two species, $\sigma = A$ and B . The two species have the same number of extra degrees of freedom I^σ , and hence have the same specific heat ratio γ^σ . And no external force is under consideration. Here, we extend the DBM to the system containing two components with independent specific heat ratios in a force field. The discrete Boltzmann equation takes the following form,

$$\frac{\partial f_i^\sigma}{\partial t} + v_{i\alpha}^\sigma \frac{\partial f_i^\sigma}{\partial r_\alpha} = \Omega_i^\sigma + G_i^\sigma, \quad (1)$$

where r_α is the Cartesian coordinate with α denoting directions; $v_{i\alpha}^\sigma$ represents the discrete velocity with $i = 1, 2, \dots, N$, and N is the total number of discrete velocities; the collision term Ω_i^σ and force term G_i^σ describe the change rates of local distribution function f_i^σ on account of the molecular collision and external force, respectively.

2.1. Collision term

Before introducing the explicit formula of the collision term, let us exhibit the physical reason for this model. The key step of physical modeling of complex fluid systems is the coarse-graining (or simplification) process. The physical quantities of our concern should remain unchanged in this process. On the whole, there are two steps in the coarse-graining process of the discrete Boltzmann modeling.

Step I: the linearization of collision term

As is well known, the original collision term Ω^σ in the continuous Boltzmann equation is too complex to be solved directly. For the sake of solving the Boltzmann equation, we resort to the approximation of Ω^σ . To be specific, the collision term is linearized as bellow,

$$\Omega^\sigma = -\frac{1}{\tau^\sigma} (f^\sigma - f^{\sigma eq}), \quad (2)$$

where $f^{\sigma eq}$ is the local equilibrium distribution function; $\tau^\sigma = 1/(n^A/\theta^A + n^B/\theta^B)$ denotes the relaxation time dependent on the particle number density

n^σ and two flexible parameters (θ^A, θ^B) [44]. Equation (2) satisfies the following condition

$$\int \int \Omega^\sigma \Psi d\mathbf{v} d\eta = \int \int -\frac{1}{\tau^\sigma} (f^\sigma - f^{\sigma eq}) \Psi d\mathbf{v} d\eta. \quad (3)$$

Here Ψ is a matrix whose elements are $\overbrace{\mathbf{v}\mathbf{v}\cdots\mathbf{v}}^\alpha \eta^{2\beta}$, which is a α -th order tensor, with $\alpha = 0, 1, \dots$, and $\beta = 0, 1, \dots$. And \mathbf{v} is the particle velocity describing translational motions, η^2 is utilized to globally describe the internal energies in extra degrees of freedom corresponding to molecular rotation and/or vibration. It should be noted [42] that the more elements the matrix Ψ has, the more complex the form of $f^{\sigma eq}$ is. Its form depends on the given elements and is different in various modes, such as, Bhatnagar-Gross-Krook (BGK) model [45], Kogan model [46], ellipsoidal statistical BGK model [47], Shakhov model [48], Rykov model [49], Liu model [50], etc. The expression of $f^{\sigma eq}$ adopted in this work reads [51]

$$f^{\sigma eq} = n^\sigma \left(\frac{m^\sigma}{2\pi kT} \right)^{D/2} \left(\frac{m^\sigma}{2\pi I^\sigma kT} \right)^{1/2} \exp \left[-\frac{m^\sigma (\mathbf{v} - \mathbf{u})^2}{2kT} - \frac{m^\sigma \eta^2}{2I^\sigma kT} \right], \quad (4)$$

where m^σ is the particle mass, $k = 1$ the Boltzmann constant, $D = 2$ the number of spatial dimensions, \mathbf{u} the hydrodynamic velocity of the system, T the temperature of the system. Mathematically, Eq. (4) is the most probable distribution in the system with given parameters $(m^\sigma, n^\sigma, \mathbf{u}, T, I^\sigma)$. From Eq. (4), we can obtain the moments of $f^{\sigma eq}$, see Eqs. (5)–(11).

Step II: the discretization of particle velocity

Equation (4), which depends on the continuous particle velocity \mathbf{v} , is still hard to be calculated. To overcome this difficulty, it is necessary to discretize the particle velocity. Note that, our concerned quantities are some kinetic moments, which should not be changed in the simplification [50]. To achieve this, the moments calculated from the summation of $f_i^{\sigma eq}$ should be consistent with those from the integration of $f^{\sigma eq}$. Specifically,

$$\int \int f^{\sigma eq} d\mathbf{v} d\eta = \sum_i f_i^{\sigma eq}, \quad (5)$$

$$\int \int f^{\sigma eq} v_\alpha d\mathbf{v} d\eta = \sum_i f_i^{\sigma eq} v_{i\alpha}^\sigma, \quad (6)$$

$$\int \int f^{\sigma eq} (v^2 + \eta^2) d\mathbf{v} d\eta = \sum_i f_i^{\sigma eq} (v_i^{\sigma^2} + \eta_i^{\sigma^2}), \quad (7)$$

$$\int \int f^{\sigma eq} v_\alpha v_\beta d\mathbf{v} d\eta = \sum_i f_i^{\sigma eq} v_{i\alpha}^\sigma v_{i\beta}^\sigma, \quad (8)$$

$$\int \int f^{\sigma eq} (v^2 + \eta^2) v_\alpha d\mathbf{v} d\eta = \sum_i f_i^{\sigma eq} (v_i^{\sigma^2} + \eta_i^{\sigma^2}) v_{i\alpha}^\sigma, \quad (9)$$

$$\int \int f^{\sigma eq} v_\alpha v_\beta v_\chi d\mathbf{v} d\eta = \sum_i f_i^{\sigma eq} v_{i\alpha}^\sigma v_{i\beta}^\sigma v_{i\chi}^\sigma, \quad (10)$$

$$\int \int f^{\sigma eq} (v^2 + \eta^2) v_\alpha v_\beta d\mathbf{v} d\eta = \sum_i f_i^{\sigma eq} (v_i^{\sigma^2} + \eta_i^{\sigma^2}) v_{i\alpha}^\sigma v_{i\beta}^\sigma, \quad (11)$$

where the integral is extended over all phase space (\mathbf{v}, η) . The above seven equations are necessary for the recovery of NS equations with flexible specific heat ratio in a force field.

To ensure conservation of mass, momentum and energy, the collision term should satisfy the following conditions

$$\sum_\sigma \int \int \Omega^\sigma d\mathbf{v} d\eta = 0 = \sum_\sigma \sum_i \Omega_i^\sigma, \quad (12)$$

$$\sum_\sigma \int \int \Omega^\sigma v_\alpha d\mathbf{v} d\eta = 0 = \sum_\sigma \sum_i \Omega_i^\sigma v_{i\alpha}^\sigma, \quad (13)$$

$$\sum_\sigma \int \int \Omega^\sigma (v^2 + \eta^2) d\mathbf{v} d\eta = 0 = \sum_\sigma \sum_i \Omega_i^\sigma (v_i^{\sigma^2} + \eta_i^{\sigma^2}). \quad (14)$$

Equations (12)-(14) mean that $f^{\sigma eq}$ and $f_i^{\sigma eq}$ can be replaced by f^σ and f_i^σ in Eqs. (5)-(7). $f^{\sigma eq}$ and $f_i^{\sigma eq}$ can not be replaced by f^σ and f_i^σ in Eqs. (8)-(11), where the differences between the results calculated by $f_i^{\sigma eq}$ and f_i^σ are due to the derivation of the system from equilibrium state, see the definition in Eqs. (31)-(34). Additionally, the discrete velocity model D2V16 is adopted in this work, see ref.[42] for more details.

2.2. Force term

In this subsection, we introduce two types of force term. The former was used in Ref. [14], the latter is presented by us.

2.2.1. Type I

As stated in Ref. [14], when the system is not too far from equilibrium state, the equilibrium distribution function $f^{\sigma seq}(n^\sigma, \mathbf{u}^\sigma, T^\sigma)$ is the leading part of the distribution function f^σ , i.e., $f^\sigma \approx f^{\sigma seq}$. Consequently,

$$G^\sigma = -\mathbf{a} \cdot \frac{\partial f^\sigma}{\partial \mathbf{v}} \approx -\mathbf{a} \cdot \frac{\partial f^{\sigma seq}}{\partial \mathbf{v}} = \frac{m^\sigma}{T^\sigma} \mathbf{a} \cdot (\mathbf{v} - \mathbf{u}^\sigma) f^{\sigma seq}, \quad (15)$$

whose discretization form is taken as

$$G_i^\sigma = \frac{m^\sigma}{T^\sigma} a_\alpha (v_{i\alpha}^\sigma - u_\alpha^\sigma) f_i^{\sigma seq}. \quad (16)$$

Here $\mathbf{a} = \sum_\alpha a_\alpha \mathbf{e}_\alpha$ represents the body acceleration, \mathbf{e}_α the unit vector in α direction.

2.2.2. Type II

On account of external force, the velocity and energy of component σ change from u_α^σ and E^σ into

$$u_\alpha^{\sigma\dagger} = u_\alpha^\sigma + \tau^\sigma a_\alpha, \quad (17)$$

$$E^{\sigma\dagger} = E^\sigma + \sum_\alpha \tau^\sigma \rho^\sigma u_\alpha^\sigma a_\alpha, \quad (18)$$

within time τ^σ . Meanwhile, the temperature of component σ becomes

$$T^{\sigma\dagger} = T^\sigma - \frac{m^\sigma}{D + I^\sigma} \tau^{\sigma 2} a_\alpha^2, \quad (19)$$

which is derived from Eqs. (17), (18) and the definition $E^\sigma = \frac{D+I^\sigma}{2} n^\sigma T^\sigma + \frac{1}{2} \rho^\sigma u^{\sigma 2}$. Hence, the force term reads

$$G_i^\sigma = \frac{1}{\tau^\sigma} [f_i^{\sigma seq}(n^\sigma, \mathbf{u}^{\sigma\dagger}, T^{\sigma\dagger}) - f_i^{\sigma seq}(n^\sigma, \mathbf{u}^\sigma, T^\sigma)]. \quad (20)$$

It is easy to demonstrate theoretically that Eqs. (16) and (20) are equivalent at the level of the first order accuracy. To perform the validation numerically, we use the two types in Eqs. (16) and (20) to simulate the motion of free fall, respectively, as seen in Fig. 1.

2.3. Kinetic properties

2.3.1. NS equations

It is easy to prove that, via the Chapman-Enskog multiscale analysis, this model could recover the NS equations in a force field in the hydrodynamic limit,

$$\frac{\partial \rho^\sigma}{\partial t} + \frac{\partial}{\partial r_\alpha} (\rho^\sigma u_\alpha^\sigma) = 0, \quad (21)$$

$$\begin{aligned} \frac{\partial}{\partial t} (\rho^\sigma u_\alpha^\sigma) + \frac{\partial}{\partial r_\beta} (\delta_{\alpha\beta} p^\sigma + \rho^\sigma u_\alpha^\sigma u_\beta^\sigma) + \frac{\partial}{\partial r_\beta} (P_{\alpha\beta}^\sigma + U_{\alpha\beta}^\sigma) \\ = \rho^\sigma a_\alpha - \frac{\rho^\sigma}{\tau^\sigma} (u_\alpha^\sigma - u_\alpha), \end{aligned} \quad (22)$$

$$\begin{aligned} \frac{\partial}{\partial t} \rho^\sigma (e^\sigma + \frac{1}{2} u^{\sigma 2}) + \frac{\partial}{\partial r_\alpha} [\rho^\sigma u_\alpha^\sigma (e^\sigma + \frac{1}{2} u^{\sigma 2}) + p^\sigma u_\alpha^\sigma] \\ - \frac{\partial}{\partial r_\alpha} \left[\kappa^\sigma \frac{\partial}{\partial r_\alpha} \left(\frac{D+I^\sigma}{2} \frac{T^\sigma}{m^\sigma} \right) - u_\beta^\sigma P_{\alpha\beta}^\sigma + X_\alpha^\sigma \right] \\ = \rho^\sigma u_\alpha^\sigma a_\alpha - \frac{\rho^\sigma}{\tau^\sigma} \left(\frac{D+I^\sigma}{2} \frac{T^\sigma - T}{m^\sigma} + \frac{u^{\sigma 2} - u^2}{2} \right), \end{aligned} \quad (23)$$

with

$$P_{\alpha\beta}^\sigma = -\mu^\sigma \left(\frac{\partial u_\alpha^\sigma}{\partial r_\beta} + \frac{\partial u_\beta^\sigma}{\partial r_\alpha} - \frac{2\delta_{\alpha\beta}}{D+I^\sigma} \frac{\partial u_\chi^\sigma}{\partial r_\chi} \right), \quad (24)$$

$$U_{\alpha\beta}^\sigma = -\rho^\sigma \left(\delta_{\alpha\beta} \frac{u^{\sigma 2} + u^2 - 2u_\chi^\sigma u_\chi}{D+I^\sigma} + u_\alpha u_\beta^\sigma + u_\alpha^\sigma u_\beta - u_\alpha^\sigma u_\beta^\sigma - u_\alpha u_\beta \right), \quad (25)$$

$$X_\alpha^\sigma = \frac{\rho^\sigma u_\alpha^\sigma}{D+I^\sigma} (u_\beta^\sigma - u_\beta)^2 - \rho^\sigma \frac{u_\alpha^\sigma - u_\alpha}{2} \left[\frac{D+I^\sigma+2}{m^\sigma} (T^\sigma - T) + u^{\sigma 2} - u^2 \right], \quad (26)$$

where $p^\sigma = n^\sigma T^\sigma$, $e^\sigma = (D+I^\sigma)T^\sigma/(2m^\sigma)$, $\mu^\sigma = p^\sigma \tau^\sigma$, $\kappa^\sigma = \gamma^\sigma \mu^\sigma$, and $\gamma^\sigma = (D+I^\sigma+2)/(D+I^\sigma)$ denote the pressure, the internal energy per unit mass, the dynamic viscosity coefficient, the heat conductivity and the specific heat ratio of species σ , respectively.

Performing the operator \sum_σ to the two sides of Eqs. (21) – (23) gives the NS equations describing the whole system,

$$\frac{\partial \rho}{\partial t} + \frac{\partial}{\partial r_\alpha} (\rho u_\alpha) = 0, \quad (27)$$

$$\frac{\partial}{\partial t} (\rho u_\alpha) + \frac{\partial}{\partial r_\beta} \sum_\sigma (\delta_{\alpha\beta} p^\sigma + \rho^\sigma u_\alpha^\sigma u_\beta^\sigma) + \frac{\partial}{\partial r_\beta} \sum_\sigma P_{\alpha\beta}^\sigma = \rho a_\alpha, \quad (28)$$

$$\frac{\partial}{\partial t} [\rho (e + \frac{1}{2}u^2)] + \frac{\partial}{\partial r_\alpha} \sum_\sigma [\rho^\sigma u_\alpha^\sigma (e^\sigma + \frac{1}{2}u^{\sigma 2}) + p^\sigma u_\alpha^\sigma] \quad (29)$$

$$- \frac{\partial}{\partial r_\alpha} \sum_\sigma \left[\kappa^\sigma \frac{\partial}{\partial r_\alpha} \left(\frac{D+I^\sigma}{2} \frac{T^\sigma}{m^\sigma} \right) - u_\beta^\sigma P_{\alpha\beta}^\sigma + X_\alpha^\sigma \right] = \rho u_\alpha a_\alpha, \quad (30)$$

where $e = \sum_\sigma \rho^\sigma (e^\sigma + u^{\sigma 2}/2)/\rho - u^2/2$ is the internal energy of the physical system per unit mass.

2.3.2. Nonequilibrium manifestations

In reality, all physical systems evolve in non-equilibrium states. The HNE and TNE behaviors play important roles in non-equilibrium systems. However, the non-equilibrium state is commonly too complex to describe. Fortunately, the DBM provides a simple tool to investigate the non-equilibrium manifestations [14, 15, 37, 38, 39, 40, 41, 42]. Specifically,

$$\Delta_2^{\sigma*} = \sum_i m^\sigma (f_i^\sigma - f_i^{\sigma eq}) \mathbf{v}_i^{\sigma*} \mathbf{v}_i^{\sigma*}, \quad (31)$$

$$\Delta_{3,1}^{\sigma*} = \sum_i m^\sigma (f_i^\sigma - f_i^{\sigma eq}) (v_i^{\sigma*2} + \eta_i^{\sigma 2}) \mathbf{v}_i^{\sigma*}, \quad (32)$$

$$\Delta_3^{\sigma*} = \sum_i m^\sigma (f_i^\sigma - f_i^{\sigma eq}) \mathbf{v}_i^{\sigma*} \mathbf{v}_i^{\sigma*} \mathbf{v}_i^{\sigma*}, \quad (33)$$

$$\Delta_{4,2}^{\sigma*} = \sum_i m^\sigma (f_i^\sigma - f_i^{\sigma eq}) (v_i^{\sigma*2} + \eta_i^{\sigma 2}) \mathbf{v}_i^{\sigma*} \mathbf{v}_i^{\sigma*}, \quad (34)$$

where $\mathbf{v}_i^{\sigma*} = \mathbf{v}_i^\sigma - \mathbf{u}$ is the particle velocity \mathbf{v}_i^σ relative to the hydrodynamic velocity \mathbf{u} .

The components of the above tensors in Eqs. (31)-(34) depend on the coordinate system. They may have different forms if the coordinate system changes. For the sake of convenience, we introduce the invariants of tensors. Let us write a tensor as Δ and its invariant as Λ . The invariant of the first order tensor whose components are Δ_α is

$$\Lambda = \sum_\alpha \Delta_\alpha \Delta_\alpha. \quad (35)$$

The independent invariants of the second order tensor having components $\Delta_{\alpha\beta}$ are

$$\Lambda_1 = \sum_\alpha \Delta_{\alpha\alpha}, \quad (36)$$

$$\Lambda_2 = \sum_{\alpha,\beta} \Delta_{\alpha\beta} \Delta_{\alpha\beta}. \quad (37)$$

The independent invariants of the third order tensor with components $\Delta_{\alpha\beta\gamma}$ are

$$\Lambda_1 = \sum_{\alpha,\beta,\gamma} \Delta_{\alpha\beta\gamma} \Delta_{\alpha\beta\gamma}, \quad (38)$$

$$\Lambda_2 = \sum_{\alpha,\beta,\gamma} \Delta_{\alpha\alpha\gamma} \Delta_{\beta\beta\gamma}, \quad (39)$$

$$\Lambda_3 = \sum_{\alpha,\beta,\gamma,\delta,\varepsilon,\zeta} \Delta_{\alpha\beta\gamma} \Delta_{\gamma\delta\varepsilon} \Delta_{\delta\varepsilon\zeta} \Delta_{\alpha\beta\zeta}. \quad (40)$$

The subscripts $\alpha, \beta, \gamma, \delta, \varepsilon, \zeta$ in Eqs. (35)-(40) stand for x or y . To be specific, the invariants of the second order tensor $\Delta_2^{\sigma*}$ are $\Lambda_1^{\sigma*}$ and $\Lambda_2^{\sigma*}$. $\Lambda_1^{\sigma*}$ is the “fluctuation of translational energy”. Physically, $\Lambda_2^{\sigma*}$ is defined as the value of “non-organized stress”, and mathematically, $\Lambda_2^{\sigma*} \geq 0$. The invariant $\Lambda^{\sigma*}$ of vector $\Delta_{3,1}^{\sigma*}$ denotes the value of “non-organized energy flux”, which is distinguishable from the “organized energy flux” $\sum_i m^\sigma f_i^{\sigma eq} (v_i^{\sigma 2} + \eta_i^{\sigma 2}) \mathbf{u}$. Here, “non-organised” is relative to “organised”. The organised behaviors refer to the collective motion of the fluid. While the non-organised ones refer to the molecular individualism on top of the collective motion [14], and play important roles in non-equilibrium systems where the energy equipartition theorem breaks.

Furthermore, the computed departures from equilibrium depend on the selected collision model [45, 46, 47, 48, 49, 50]. The collision models are at different levels of approximating the original collision term of the Boltzmann equation, which is also an approximation of the complex real system. Consequently, the accuracy of all simulation results is limited at a certain level [42, 43].

3. Numerical simulation and investigation

In this section, we conduct the numerical verification of this model firstly. Then, we use it to probe the dynamic process of RT instability. For cases without gravitation, the numerical verifications are referred to our previous work[42]. For cases with gravitation, we verify the model via simulating free fall of the system.

3.1. Free fall

For the sake of testing the effect of external force, the motion of free fall is simulated here. The simulation is performed on a $N_x \times N_y = 1 \times 400$ grid,

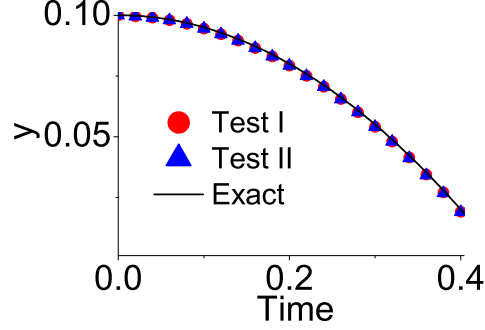


Figure 1: The motion of free fall: Test I (circles), Test II (triangles), and the exact solution (line).

with spatial step $\Delta x = \Delta y = 5 \times 10^{-4}$ and temporal step $\Delta t = 10^{-5}$. The computational region is initially divided into two halves. The upper half is filled with medium A and the lower B . The pressure $p = 1$ is uniform in the whole region. The temperature in the upper (lower) part is $T_u = 1$ ($T_d = 2$). The particle number density of species A and B is p/T_u and p/T_d , respectively. Other parameters are $a_x = 0$, $a_y = -1$, $m^\sigma = 1$, $\theta^\sigma = 1.5 \times 10^{-5}$, $I^\sigma = 3$, $(v_a^\sigma, v_b^\sigma, v_c^\sigma, v_d^\sigma, \eta_a^\sigma) = (0.6, 1.1, 2.1, 2.9, 1.9)$. Moreover, boundary conditions for this simulation are as follows: the periodic boundary conditions are employed in the horizontal direction, the inflow/outflow boundary conditions in the vertical direction. Figure 1 delineates the motion of free fall. Tests I and II denote the DBM simulations using formulae (16) and (20), respectively. The exact solution is $y = 0.1 + 0.5a_y t^2$. Clearly, all results are in nice agreement.

3.2. RT instability

Now, the proposed DBM is used to investigate the RT instability. Initially, the physical field is on the hydrostatic unstable equilibrium, i.e.,

$$\nabla p = \rho \mathbf{a}, \quad (41)$$

where $a_x = 0$ and $a_y = -g$, with g the value of gravitational acceleration. Equation (41) means that the pressure increases monotonously from top to bottom. The value (direction) of the pressure gradient is equal (opposite) to

that of gravity. To satisfy this condition, two kinds of configuration are proposed as below,

$$\begin{cases} T(y) = T_u, n^A(y) = \frac{p_m}{T_u} \exp\left[\frac{m^A g}{T_u}(y_m - y)\right], n^B(y) = 0, y > y_m, \\ T(y) = T_d, n^B(y) = \frac{p_m}{T_d} \exp\left[\frac{m^B g}{T_d}(y_m - y)\right], n^A(y) = 0, y < y_m, \end{cases} \quad (42)$$

or

$$\begin{cases} n^A(y) = n_u, n^B(y) = 0, T(y) = m^A g(y_m - y) + \frac{p_m}{n_u}, y > y_m, \\ n^B(y) = n_d, n^A(y) = 0, T(y) = m^B g(y_m - y) + \frac{p_m}{n_d}, y < y_m, \end{cases} \quad (43)$$

where the subscripts u and d denote the upper and lower halves of the physical domain, m represents the material interface. Considering the transition layer between the two parts, the field jump at the interface is smoothed by a tanh profile with width W . Specifically, the initial temperature profile is chosen to be $T(y) = (T_u + T_d)/2 + (T_u - T_d)/2 \times \tanh((y - y_m)/W)$ in Eq. (42), and the initial densities take the forms $n^A(y) = n_u/2 + n_u/2 \times \tanh((y - y_m)/W)$, $n^B(y) = n_d/2 - n_d/2 \times \tanh((y - y_m)/W)$ in Eq. (43). A half single-mode sinusoidal perturbation with amplitude A_0 is imposed on the interface, i.e., $y_m = L_y/2 + A_0 \times \cos(\pi x/L_x)$. Here L_x and L_y are the width and length of the computational domain, respectively. Furthermore, the symmetrical boundary conditions are adopted in the x direction, the specular reflection boundary conditions in the y direction.

As conducted in previous works [14, 15], the DBMs for single component systems can only be used to simulate RT instability in a special situation with superposition of a heavy cold medium above a hot light one. While our improved DBM for bi-component systems has the capability of investigating RT instability in more practical cases where the two media have independent temperature. Consequently, this model can be used to study effects of various temperature differences between them. In this work, the case of a uniform initial temperature field is investigated, which is beyond the capability of DBMs for single component systems [14, 15]. Moreover, compared with the DBMs for single component systems [14, 15], this model is capable of obtaining more details of the flow field, such as the density, hydrodynamic velocity, temperature, and pressure of each

Cases	Re	θ^σ	Δt	$\Delta x = \Delta y$	$(v_a^A, v_b^A, v_c^A, v_d^A, \eta_a^A)$ $(v_a^B, v_b^B, v_c^B, v_d^B, \eta_a^B)$
Run I	2000	1.262×10^{-4}	5×10^{-6}	4×10^{-4}	(5.5, 2.5, 0.7, 0.9, 5.3) (6.0, 2.7, 0.2, 0.5, 6.3)
Run II	500	5.046×10^{-4}	2×10^{-5}	8×10^{-4}	(4.5, 2.2, 0.2, 0.5, 5.3) (6.0, 2.7, 0.3, 0.9, 6.3)
Run III	125	2.018×10^{-3}	4×10^{-5}	1×10^{-3}	(4.5, 2.2, 0.2, 0.5, 5.3) (6.0, 2.7, 0.3, 0.9, 6.3)

Table 1: Parameters used in the three runs of RT instability.

component.

Let us consider the initial configuration described by Eq. (42), where both heavy and light media have the same temperature, $T_u = T_d = 1.0$. Three runs with various dynamic viscosities of the fluid are carried out. The parameters are $m^A = 3$, $m^B = 1$, $W = L_y/200$, $A_0 = L_y/100$, $p_m = 40$, $g = 2$, $I^\sigma = 3$, $L_x \times L_y = 0.1 \times 1.0$, the other parameters are given in Table 1. The Reynolds number is a function of the space and time in compressible flows. To roughly investigate the Reynolds effects, in this work we define the Reynolds number as $Re = \bar{\rho} \bar{u} \bar{L} / \bar{\mu}$. The characteristic length is $\bar{L} = \lambda$, characteristic velocity $\bar{u} = \sqrt{g/k}$, and the wave number $k = 2\pi/\lambda$. The characteristic density $\bar{\rho} = \sum_\sigma m^\sigma n_m^\sigma M_m^\sigma$, the dynamic viscosity $\bar{\mu} = p_m \tau_m$, the relaxation time $\tau_m = (\sum_\sigma n_m^\sigma Y_m^\sigma \theta^{\sigma-1})^{-1}$, the particle number density n_m^σ , mole fraction Y_m^σ , and pressure p_m^σ are initially located at the material interface. Hence, the Reynolds numbers in the three runs are $Re = 2000$, 500, and 125, respectively.

Figure 2 depicts the contours of mole fraction $Y^A (= n^A/n)$ in the evolution of RT instability. Subplots (a)-(d) are for $Re = 2000$, (e)-(h) for $Re = 500$, (i)-(l) for $Re = 125$. In each case, we show the snapshots at times $t = 0.0, 0.4, 1.2$, and 2.00, respectively. The initial mole fraction fields are the same in the three

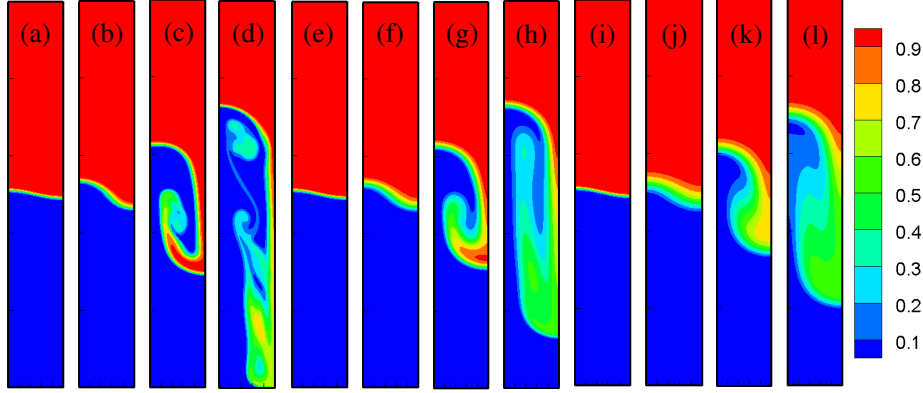


Figure 2: Contours of mole fraction Y^A in the evolution of RT instability with various Reynolds numbers at times $t = 0.0, 0.4, 1.2$, and 2.00 , respectively. (a)-(d) are for $Re = 2000$, (e)-(h) for $Re = 500$, (i)-(l) for $Re = 125$.

runs. The following three points can be obtained. (i) At the initial stage, the movements of the two media are symmetrical. Later, the material interface gets farther and farther away from the sinusoidal shape. The heavy fluid drops down and forms a spike with time, while the light one rises up with the formation of a bubble. And the two media penetrate into each other as time advances. (ii) With the opposite movements of them, the Kelvin-Helmholtz (KH) instability [52, 53, 54, 55] takes place when there is a difference between the tangential velocities across the material interface. Owing to the KH instability, the spike rolls up and the mushroom structure occurs, which promotes the mixing rate of the two fluids. (iii) With the increasing of dynamic viscosity (i.e., with the decreasing of Re), the width of the material interface increases faster and the friction between the two media enhances, the KH instability is suppressed and has a relatively weak effect, the vortex is weak and the downward-moving spike becomes slow, the structure of spike is smoothed and the material interface appears symmetrical between the upper and lower parts.

Figure 3 illustrates the heights (a) and velocities (b) of bubble and spike fronts in the evolution of RT instability. The lines with squares, upper triangles, and lower triangles stand for the simulation results from runs of $Re = 2000, 500$,

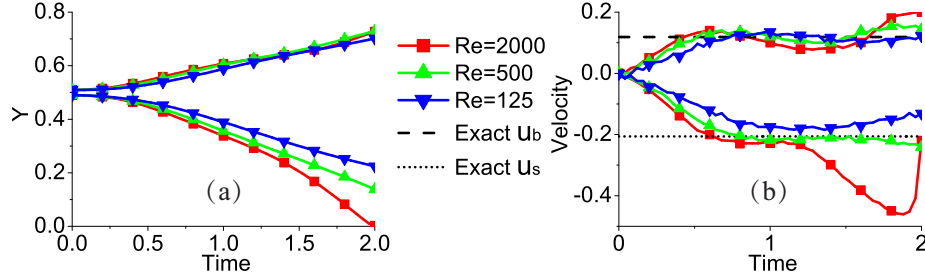


Figure 3: The heights (a) and velocities (b) of bubble and spike fronts versus time. The lines with symbols are for simulation results, the dashed and dotted lines are for exact results.

and 125, respectively. The dashed and dotted lines represent the exact results of bubble and spike velocities calculated by the classic potential flow model [10]. Specifically,

$$u_b = \sqrt{\frac{2A_t g}{C_g k (1 + A_t)}}, \quad (44)$$

$$u_s = \sqrt{\frac{2A_t g}{C_g k (1 - A_t)}}, \quad (45)$$

where $A_t = (\rho^A - \rho^B)/(\rho^A + \rho^B)$ represents the Atwood number, $C_g = 3$ and 1 are for the two- and three-dimensional geometries, respectively. The following four points are clear from the plots. (i) In the three runs, the bubble goes up and the spike drops down until they reach the box wall. The bubble fronts are close to each other in the three runs while the spike fronts fall down fast at high Reynolds number. (ii) The speeds of bubble and spike fronts linearly increase in the early stage, then level off in the subsequent period of time when the numerical results are close to the exact solutions. (iii) For high Reynolds number ($Re = 2000$), there are three distinctive stages of the spike speed, i.e., acceleration ($0 \leq t < 0.6$), plateau ($0.6 \leq t < 1.2$), and re-acceleration ($1.2 \leq t < 1.9$) stages. The bubble speed shows similar behaviours. (iv) For low Reynolds number ($Re = 125$), there is no re-acceleration stage in the evolution of the bubble and spike speeds. Physically, the re-acceleration is caused by the vortex on account of the KH instability, which is suppressed by a large viscosity.

3.3. Invariants of tensors

The invariants of tensors in Eqs. (31)-(34) are independent of coordinate systems and have a physical significance to the thermodynamic non-equilibrium investigation. However, they have never been studied. Now let us probe them in the process of RT instability.

First, we investigate the invariant $\Lambda_1^{\sigma*}$ of the tensor $\Delta_2^{\sigma*}$. Figure 4 illustrates the contours of Λ_1^{A*} (a)-(d) and Λ_1^{B*} (e)-(h) in the case of $Re = 2000$ at times $t = 0.04, 0.4, 1.2$, and 2.0 , respectively. It can be found in Fig. 4 that the topological structures of Λ_1^{A*} and Λ_1^{B*} are quite similar. Physically, the two invariants are (non-) zero where the system is in (non-) equilibrium state. Around the material interface where the physical gradients are sharp, the system deviates from the equilibrium state obviously, and the values of the invariants have large departure from zero. Moreover, the areas for $\Lambda_1^{\sigma*} \neq 0$ increase as the material interface is enlarged in the evolution of RT instability. And $\Lambda_1^{\sigma*}$ increases dramatically when the interface reaches the bottom. In addition, $\Lambda_1^{\sigma*}$ is positive or negative in non-equilibrium state. That is to say, the translational energies $\sum_i m^\sigma f_i^\sigma v_{i\alpha}^{\sigma*} v_{i\alpha}^{\sigma*}$ is greater or less than the one $\sum_i m^\sigma f_i^{\sigma eq} v_{i\alpha}^{\sigma*} v_{i\alpha}^{\sigma*}$ where the energy equipartition theorem breaks.

Let us probe the integration results of the absolute values of the “fluctuation of translational energies” $|\Lambda_1^{\sigma*}|$, which reflect the global thermodynamic non-equilibrium intensity. Figure 5 gives the evolution of $\int \int |\Lambda_1^{\sigma*}| dx dy$, where the integral extends over the whole computational domain. Panels (a)-(c) are for the runs of $Re = 2000, 500$, and 125 , respectively. It can be found that Λ_1^{A*} and Λ_1^{B*} show similar trends. For high Reynolds number, there are roughly two stages, i.e., the first increasing and afterwards decreasing trends, in the whole process. In contrast, there are three stages for low Reynolds number, i.e., the first decreasing trend, then increasing trend, and finally decreasing trend. For all cases, the non-equilibrium manifestations approach zero when the mixing between media is finally saturated. In fact, there are competitive effects on non-equilibrium manifestations in the process of RT instability. Mathematically, the global thermodynamic non-equilibrium intensity increases with the increasing

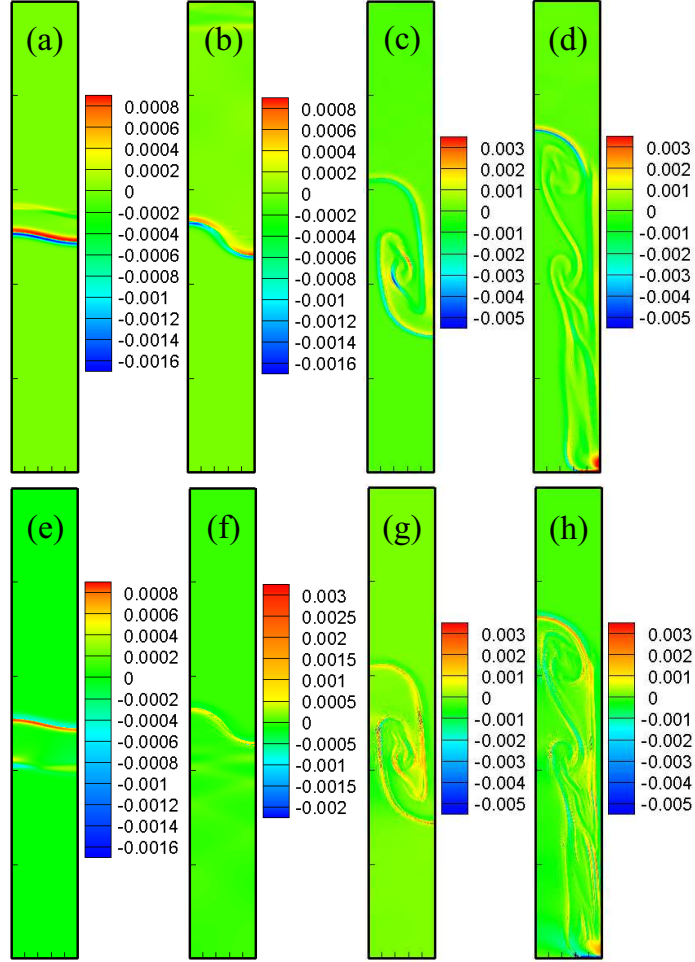


Figure 4: Contours of invariant $\Lambda_1^{\sigma*}$ of the tensor $\Delta_2^{\sigma*}$ in the case of $Re = 2000$ at times $t = 0.04, 0.4, 1.2$, and 2.0 , from left to right, respectively. The first row is for Λ_1^{A*} , the second for Λ_1^{B*} .

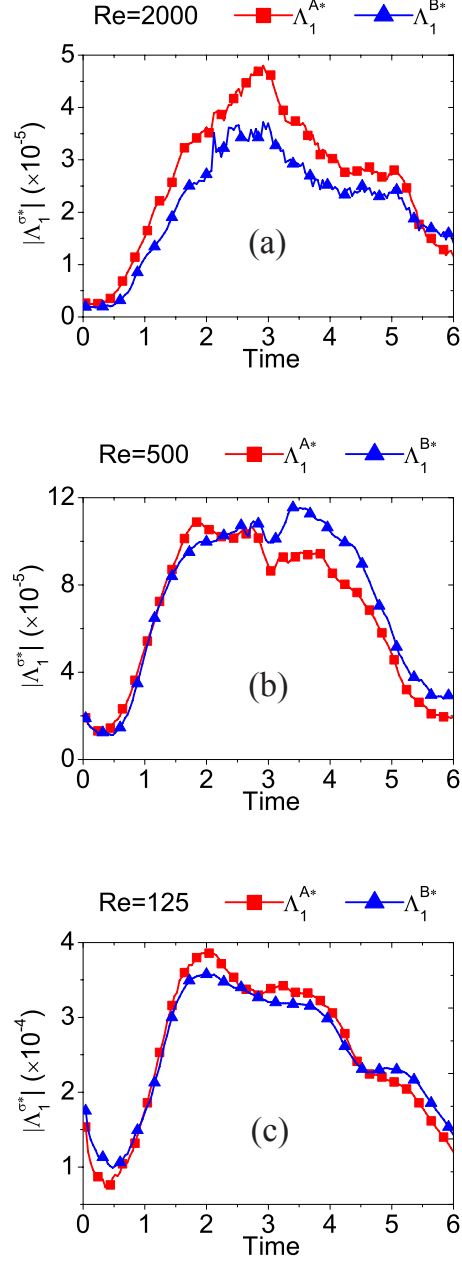


Figure 5: The evolution of $\int \int |\Lambda_1^{A*}| dx dy$ (squares) and $\int \int |\Lambda_1^{B*}| dx dy$ (triangles). Here $\Lambda_1^{\sigma*}$ is the invariant of the tensor $\Delta_2^{\sigma*}$. Panels (a)-(c) are for $Re = 2000$, 500 , and 125 , respectively.

non-equilibrium area, relaxation time and values of physical gradients [42]. As time goes on, the non-equilibrium area enlarges, the physical gradients become smoothed. Consequently, the values of $\int \int |\Lambda_1^{\sigma*}| dx dy$ show different tendencies in the whole process.

As shown in Fig. 5, for lower Reynolds number (i.e., larger relaxation time), (i) the global non-equilibrium manifestations have less frequent oscillation, (ii) TNEs have stronger global effects on the whole region, (iii) they are much larger at the initial instant, and subsequently have a more obvious reducing tendency in the early stage. Physically, for larger relaxation time, the transport coefficients (including the dynamic viscosity coefficient and the heat conductivity) are larger, the corresponding transportation processes become faster, so it is easy for the system to depart far from the equilibrium state and it takes long time for the system to reach the local equilibrium state. Meanwhile, the fast transportation processes smooth the physical gradients quickly, hence the non-equilibrium effects weaken fast as well.

To obtain a comprehensive view of the non-equilibrium behaviors, we investigate the integration of the absolute values of the “non-organized energy flux” $\Lambda^{\sigma*}$, which is the invariant of vector $\Delta_{3,1}^{\sigma*}$. Figure 6 illustrates the evolution of $\int \int |\Lambda^{\sigma*}| dx dy$, where the integral extends over the whole computational domain. Panels (a)-(c) are for the runs of $Re = 2000, 500$, and 125 , respectively. Comparing Figs. 5 and 6 gives the following points.

(i) The results of $\int \int |\Lambda_1^{\sigma*}| dx dy$ in Fig. 5 and those of $\int \int |\Lambda^{\sigma*}| dx dy$ in Fig. 6 demonstrate similar trends. For low Reynolds number, there are three obviously different stages, i.e., reducing, increasing and then decreasing trends. For high Reynolds number, those non-equilibrium manifestations are weakened, and the early reducing trend is particularly suppressed and even eliminated. Hence, with increasing Reynolds number, the three tendencies may be reduced to two ones (increasing and decreasing tendencies) in the whole process. For all cases, the non-equilibrium manifestations approach to zero when the mixing between media reaches saturation finally. The physical reasons for the manifestations in Fig. 6 are similar to those in Fig. 5.

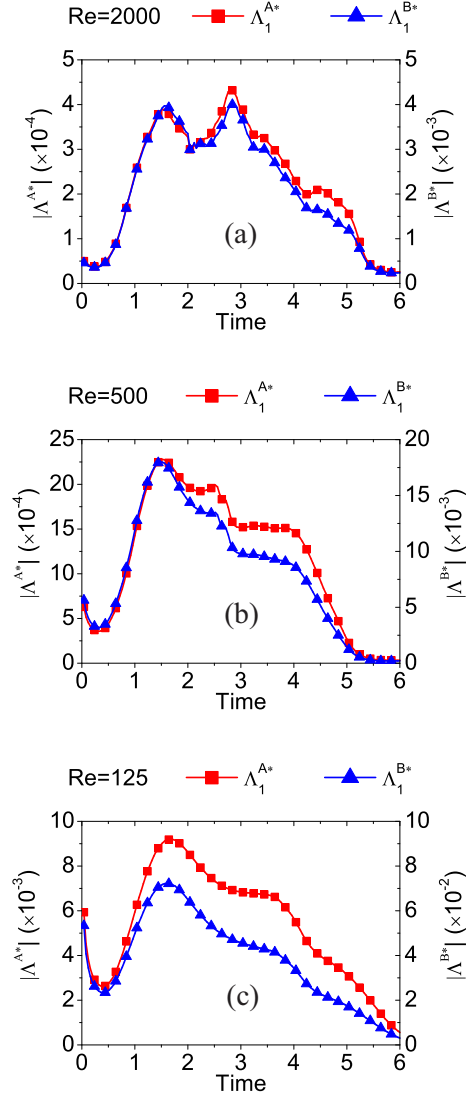


Figure 6: The evolution of $\int \int |\Lambda^{A*}| dx dy$ (squares) and $\int \int |\Lambda^{B*}| dx dy$ (triangles). Here $\Lambda^{\sigma*}$ is the invariant of the tensor $\Delta_{3,1}^{\sigma*}$. Panels (a)-(c) are for $Re = 2000, 500$, and 125 , respectively.

(ii) The values of $\int \int |\Lambda_1^{A*}| dx dy$ and $\int \int |\Lambda_1^{B*}| dx dy$ in Fig. 5 are close to each other on the same order of magnitude. While, in Fig. 6, although the results of $\int \int |\Lambda^{B*}| dx dy$ are qualitatively similar to $\int \int |\Lambda^{A*}| dx dy$, the former is an order of magnitude smaller than the latter. The physical reason needs to be studied in future.

It is worth mentioning that, the invariants ($\Lambda_1^{\sigma*}$, $\Lambda_2^{\sigma*}$, $\Lambda_3^{\sigma*}$) of the tensor $\Delta_3^{\sigma*}$ have behaviours quite similar to those in Fig. 6 (not shown here). In addition, since non-equilibrium manifestations are obvious for sharp physical gradients [42], the initial non-equilibrium manifestations enhance with reducing initial interface width W .

3.4. Entropy of mixing

Compared with the LBM/DBM for single component systems, this model has the capability of investigating entropy of mixing,

$$S = - \sum_{\sigma} n^{\sigma} \ln Y^{\sigma}. \quad (46)$$

In thermodynamics, the entropy of mixing is a portion of the total entropy. It increases when several separate parts of components are mixed without chemical reaction before the establishment of a new thermodynamic equilibrium state in a closed system. Entropy is of great concern and interest to both physicists and engineers. Here, we investigate the RT instability from the view point of the entropy of mixing.

Figure 7 exhibits the snapshots of entropy of mixing in the case of $Re = 2000$ at times $t = 0.04, 0.4, 1.2$, and 2.0 , from left to right, respectively. It can be found that the area for $S > 0$ enlarges as the material interface widens and lengthens with time. To have a quantitative study, we calculate $\int \int S dx dy$ where the integral is extended over the whole region. Figure 8 depicts the entropy of mixing $\int \int S dx dy$ (a) and its growth rate (b) in the three runs of RT instability.

It is clear in Fig. 8 (a) that the entropy of mixing increases monotonously as the two miscible media mix in the evolution of RT instability. In Fig. 8 (b), the

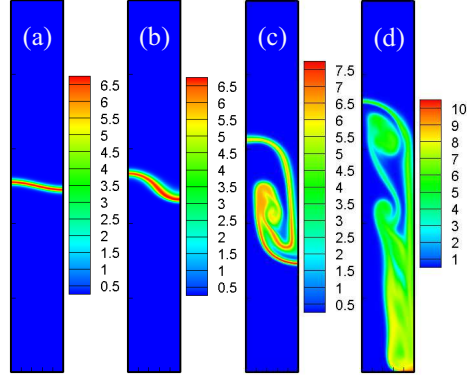


Figure 7: Snapshots of entropy of mixing in the case of $Re = 2000$ at times $t = 0.04, 0.4, 1.2,$ and 2.0 , from left to right, respectively.

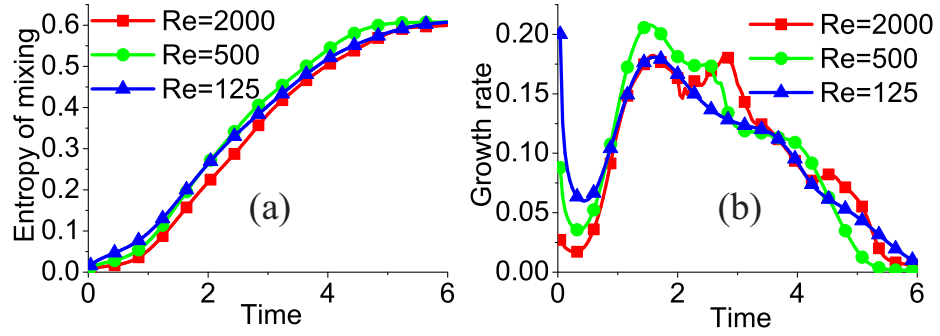


Figure 8: Entropy of mixing $\int \int S dx dy$ (a) and its growth rate (b).

growth rate of entropy of mixing shows decreasing, increasing, and then decreasing trends in three different stages. For large Reynolds number, the reducing growth rate in the early stage is particularly suppressed and even eliminated because of the slow diffusion. Physically, there are competitive mechanisms between the decreasing values of gradients particle number density and increasing area of material interface in the mixing process. Initially, the values of gradients are large, and the diffusion between the two media is quick. In the mixing process, the decreasing values of gradients make the mixing slow, while the increasing contact area between the two media makes the mixing quick. Finally, the mixing becomes slow again when the mixing starts to saturate.

In the initial stage, from $t = 0.0$ to about 0.5, both the entropy of mixing and its growth rate are higher for large viscosity (low Reynolds number) than for small viscosity (high Reynolds number). Afterwards, the rates in the three runs complete with each other. Finally, the entropies of mixing in the three runs coincide with each other and all the growth rates approach zero when the media are adequately mixed. Physically, the growth rate is high and the diffusion is fast when the viscosity of the two media is high. And the viscosity dominates in the early stage. In addition, for large viscosity, the diffusion process is fast, and the physical gradients are smoothed quickly which makes the mixing slow. Furthermore, for large viscosity, the evolution of RT instability becomes slow in the later stage, and the growth rate of the contact area reduces, which decreases the mixing growth rate.

4. Conclusions and Discussions

A DBM is proposed for a system containing two components in a gravitational field. The two components, which can have different specific heat ratios, are described by two coupled discrete Boltzmann equations. The discrete equilibrium distribution functions are calculated from the hydrodynamic velocity and temperature of the whole system, and the density of each species. Two types of force term, which are equivalent at the level of the first order accuracy,

are introduced to describe the gravitational effects. The discrete velocities for the two discrete Boltzmann equations are independent. This flexibility can be used to improve the numerical robustness. This model is validated and verified both theoretically and numerically. Theoretically, the NS equations can be obtained from this model via the Chapman-Enskog multiscale analysis. Numerically, the DBM results are consistent with the exact solutions in the simulation of free fall.

In this work, the DBM is used to investigate the non-equilibrium RT instability at three Reynolds numbers. We prove the global effects of thermodynamic non-equilibrium manifestations, including the “fluctuation of translational energies” and “non-organized energy flux”, in the computational space. For low Reynolds number, those non-equilibrium manifestations show decreasing, increasing, and then decreasing trends. For high Reynolds number, they are weakened, and the early reducing trend is particularly suppressed and even eliminated. It is interesting to find that the growth rate of the entropy of mixing demonstrates behaviors similar to the global effects of those non-equilibrium manifestations. This is because there are competitive effects on the non-equilibrium manifestations and the growth of the entropy of mixing in the process: (i) the increasing material interface enhances them; (ii) the reducing physical gradients weaken them; (iii) the fast diffusion enlarges them; (iv) the large viscosity suppresses the growth of material interface.

Apart from its capability of an NS model describing the fluid flows, the DBM can also be used to probe more details of hydrodynamic and thermodynamic non-equilibrium manifestations. And we introduce some significant invariants of tensors of those non-equilibrium manifestations. Moreover, the comparison between the DBM and the traditional models based on NS or Euler equations could be studied in future. And phenomena of the non-equilibrium RT instability in three-dimensional systems and at a much higher Reynolds number may be further investigated as well.

Acknowledgements

The authors thank Drs. Huilin Lai, Yanbiao Gan, Zhipeng Liu, Yudong Zhang, Linlin Fei and Tong Yao for fruitful discussions. AX and GZ acknowledge support of the Foundation of LCP, National Natural Science Foundation of China [under Grant No. 11475028]. KL and CL acknowledge support from the Center for Combustion Energy at Tsinghua University. YL and CL acknowledge support of National Natural Science Foundation of China [under Grant Nos. 11574390, 41472130, and 11374360], National Basic Research Program of China [under Grant No. 2013CBA01504].

References

- [1] L. Rayleigh, Investigation of the character of the equilibrium of an incompressible heavy fluid of variable density, Proc. London Math. Soc. s1-14, 170-177 (1882).
- [2] G. Taylor, The instability of liquid surfaces when accelerated in a direction perpendicular to their planes. I, Proc. R. Soc. Lond. A 201, 192-196 (1950).
- [3] S. Chandrasekhar, *Hydrodynamic and Hydromagnetic Stability*, Oxford University Press, London, 1968.
- [4] J. D. Lindl, P. Amendt, R. L. Berger, et al. The physics basis for ignition using indirect-drive targets on the National Ignition Facility, Physics of Plasmas, 11, 339-491 (2004).
- [5] B. A. Remington, R. P. Drake, D. D. Ryutov, Experimental astrophysics with high power lasers and Z pinches, Rev. Mod. Phys. 78, 755 (2006).
- [6] Y. Jiang, S. W. Davis, J. M. Stone. Nonlinear Evolution of Rayleigh-Taylor Instability in a Radiation-supported Atmosphere, The Astrophysical Journal, 763, 102 (2013).
- [7] L. Debnath, *Nonlinear water waves*, Academic Press, Boston, 1994.

- [8] M. A. Patterson, R. D. Reitz, Modeling the effects of fuel spray characteristics on diesel engine combustion and emission. SAE Technical Paper, 980131, (1998).
- [9] Vladimirova N, Rosner R. Model flames in the Boussinesq limit: the effects of feedback. *Physical Review E*, 67, 066305 (2003).
- [10] V. N. Goncharov, Analytical model of nonlinear, single-mode, classical Rayleigh-Taylor instability at arbitrary Atwood numbers. *Phys. Rev. Lett.*, 88, 134502 (2002).
- [11] L. Wang, W. Ye, Y. Li, Combined effect of the density and velocity gradients in the combination of Kelvin-Helmholtz and Rayleigh-Taylor instabilities, *Phys. Plasmas*, 17, 042103 (2010).
- [12] D. J. Lewis, The instability of liquid surfaces when accelerated in a direction perpendicular to their planes. II//*Proceedings of the Royal Society of London A: Mathematical, Physical and Engineering Sciences*. The Royal Society, 202, 81-96 (1950).
- [13] D. H. Olson, J. W. Jacobs, Experimental study of Rayleigh-Taylor instability with a complex initial perturbation, *Phys. Fluids* 21, 034103 (2009).
- [14] H. Lai, A. Xu, G. Zhang, Y. Gan, Y. Ying, and S. Succi, Thermohydrodynamic non-equilibrium effects on compressible Rayleigh-Taylor instability, *Phys. Rev. E.*, 94, 023106 (2016).
- [15] F. Chen, A. Xu, G. Zhang. Viscosity, heat conductivity, and Prandtl number effects in the Rayleigh-Taylor Instability. *Frontiers of Physics*, 11, 114703 (2016).
- [16] I. Sagert, W. Bauer, D. Colbry, et al. Kinetic Simulations of Rayleigh-Taylor Instabilities//*Journal of Physics: Conference Series*. IOP Publishing, 535, 012032 (2014).

- [17] S. Succi, *The Lattice Boltzmann Equation for Fluid Dynamics and Beyond*, Oxford University Press, New York, 2001.
- [18] R. Benzi, M. Sbragaglia, M. Bernaschi, and S. Succi, Phase-field model of long-time glasslike relaxation in binary fluid mixtures, *Phys. Rev. Lett.* 106, 164501 (2011).
- [19] A. J. Wagner, J. M. Yeomans, Spinodal decomposition in two-dimensional binary fluids, *International Journal of Modern Physics C*, 1998, 9(08): 1373-1382.
- [20] R. Ledesma-Aguilar, D. Vella, and J. M. Yeomans, Lattice-Boltzmann simulations of droplet evaporation, *Soft Matter* 10, 8267-8275 (2014).
- [21] Y. Liu, L. Moevius, X. Xu, T. Qian, J. M. Yeomans and Z. Wang, Pancake bouncing on superhydrophobic surfaces, *Nat. Phys.* 10, 515-519 (2014).
- [22] A. Montessori, P. Prestininzi, M. La Rocca, G. Falcucci, and S. Succi, Lattice kinetic approach to non-equilibrium flows//INTERNATIONAL CONFERENCE OF NUMERICAL ANALYSIS AND APPLIED MATHEMATICS 2015 (ICNAAM 2015). AIP Publishing, 1738, 090005 (2016).
- [23] He X, Zhang R, Chen S, et al. On the three-dimensional Rayleigh-Taylor instability. *Phys. Fluids*, 11, 1143-1152 (1999).
- [24] Zhang R, He X, Chen S. Interface and surface tension in incompressible lattice Boltzmann multiphase model. *Computer Physics Communications*, 129, 121-130 (2000).
- [25] Clark T T. A numerical study of the statistics of a two-dimensional Rayleigh-Taylor mixing layer. *Physics of Fluids*, 15, 2413-2423 (2003).
- [26] Nourgaliev R R, Dinh T N, Theofanous T G, et al. The lattice Boltzmann equation method: theoretical interpretation, numerics and implications. *International Journal of Multiphase Flow*, 29, 117-169 (2003).

- [27] Chiappini D, Bella G, Succi S, et al. Improved lattice Boltzmann without parasitic currents for Rayleigh-Taylor instability. *Communications in Computational Physics*, 7, 423 (2010).
- [28] Scagliarini A, Biferale L, Sbragaglia M, et al. Lattice Boltzmann methods for thermal flows: Continuum limit and applications to compressible Rayleigh-Taylor systems. *Phys. Fluids*, 22, 055101 (2010).
- [29] Biferale L, Mantovani F, Sbragaglia M, et al. Second-order closure in stratified turbulence: Simulations and modeling of bulk and entrainment regions. *Physical Review E*, 84, 016305 (2011).
- [30] Q. Li, K. H. Luo, Y. J. Gao, Y. L. He. Additional interfacial force in lattice Boltzmann models for incompressible multiphase flows, *Phys. Rev. E.*, 85, 026704 (2012).
- [31] Liu G, Guo Z. Effects of Prandtl number on mixing process in miscible Rayleigh-Taylor instability: a lattice Boltzmann study. *International Journal of Numerical Methods for Heat & Fluid Flow*, 23, 176-188 (2013).
- [32] Liang H, Shi B C, Guo Z L, et al. Phase-field-based multiple-relaxation-time lattice Boltzmann model for incompressible multiphase flows. *Physical Review E*, 89, 053320 (2014).
- [33] Liang, H., Li, Q.X., Shi, B.C., Chai, Z.H.: Lattice Boltzmann simulation of three-dimensional Rayleigh-Taylor instability. *Phys. Rev. E*. 93, 033113 (2016).
- [34] Nie X, Qian Y H, Doolen G D, et al. Lattice Boltzmann simulation of the two-dimensional Rayleigh-Taylor instability. *Phys. Rev. E.*, 58, 6861-6864 (1998).
- [35] Zu Y Q, He S. Phase-field-based lattice Boltzmann model for incompressible binary fluid systems with density and viscosity contrasts. *Physical Review E*, 87, 043301 (2013).

- [36] A. Xu, G. Zhang, Y. Gan, F. Chen, and X. Yu, Lattice Boltzmann modeling and simulation of compressible flows, *Front. Phys.* 7, 582-600 (2012).
- [37] A. Xu, G. Zhang, Y. Ying, Progress of discrete Boltzmann modeling and simulation of combustion system (in chinese), *Acta. Phys. Sin.* 64, 184701 (2015).
- [38] C. Lin, A. Xu, G. Zhang, Y. Li, S. Succi, Polar-coordinate lattice Boltzmann modeling of compressible flows, *Phys. Rev. E* 89 (2014) 013307.
- [39] C. Lin, A. Xu, G. Zhang, Y. Li, Polar Coordinate Lattice Boltzmann Kinetic Modeling of Detonation Phenomena, *Commun. Theor. Phys.* 62 (2014) 737-748.
- [40] A. Xu, C. Lin, G. Zhang and Y. Li, Multiple-relaxation-time lattice Boltzmann kinetic model for combustion, *Phys. Rev. E* 91 (2015) 043306.
- [41] Y. Gan, A. Xu, G. Zhang, and S. Succi, Discrete Boltzmann modeling of multiphase flows: hydrodynamic and thermodynamic non-equilibrium effects, *Soft Matter* 11 (2015) 5336-5345.
- [42] C. Lin, A. Xu, G. Zhang, Y. Li, Double-distribution-function discrete Boltzmann model for combustion, *Combust. Flame* 164 (2016) 137-151.
- [43] Zhang Y, Xu A, Zhang G, et al. Kinetic modeling of detonation and effects of negative temperature coefficient, *Combust. Flame* 173 (2016) 483-492.
- [44] V. Sofonea and R. F. Sekerka, BGK models for diffusion in isothermal binary fluid systems, *Physica A* 299 (2001) 494-520.
- [45] P. L. Bhatnagar, E. P. Gross and M. Krook, A model for collision processes in gases. I. Small amplitude processes in charged and neutral one-component systems, *Physical review*, 94 (1954) 511-525.
- [46] M. N. Kogan. On the equations of motion of a rarefied gas. *J. Appl. Math. Mech.*, 22 (1958) 597-607.

- [47] J. Meng, Y. Zhang, N. G. Hadjiconstantinou, G. A. Radtke, and X. Shan, Lattice ellipsoidal statistical BGK model for thermal non-equilibrium flows, *J. Fluid Mech.* 718 (2013) 347-370.
- [48] E. M. Shakhov, Generalization of the Krook kinetic relaxation equation, *Fluid Dyn.* 3 (1968) 95-96.
- [49] V. A. Rykov, A model kinetic equation for a gas with rotational degrees of freedom, *Fluid Dyn.* 10 (1975) 959-966.
- [50] G. Liu, A method for constructing a model form for the Boltzmann equation, *Phys. Fluids A*, 2 (1990) 277-280.
- [51] M. Watari, Finite difference lattice Boltzmann method with arbitrary specific heat ratio applicable to supersonic flow simulations, *Physica A* 382 (2007) 502-522.
- [52] W. Thomson, Hydrokinetic solutions and observations. *Philos. Mag. Ser.* 4, 42 (1871) 362-377.
- [53] Hermann von Helmholtz: On discontinuous movements of fluids. *Philos. Mag. Ser.* 4, 1868, 36(244): 337-346.
- [54] L. Wang, A. Teng, W. Ye, et al. Velocity gradient in Kelvin-Helmholtz instability for supersonic fluid(in chinese), *Acta. Phys. Sin.*, 58 (2009): 8426-8431.
- [55] Y. Gan, A. Xu, G. Zhang, and Y. Li. Lattice Boltzmann study on Kelvin-Helmholtz instability: Roles of velocity and density gradients. *Phys. Rev. E*, 2011, 83(5): 056704.